

Wavelet Packet Denoising of Magnetic Resonance Images: Importance of Rician Noise at Low SNR

John C. Wood¹ and Kevin M. Johnson^{2*}

Wavelet packet analysis is a mathematical transformation that can be used to post-process images, for example, to remove image noise ("denoising"). At a very low signal-to-noise ratio (SNR < 5), standard magnitude magnetic resonance images have skewed Rician noise statistics that degrade denoising performance. Since the quadrature images have approximately Gaussian noise, it was postulated that denoising would produce better contrast and sharper edges if performed before magnitude image formation. Signal-to-noise ratio (SNR), contrast-to-noise ratio (CNR), and edge blurring effects of these two approaches were examined in synthetic, phantom, and human MR images. While magnitude and complex denoising both significantly improved SNR and CNR, complex denoising yielded sharper edges and better low-intensity feature contrast. *Magn Reson Med* 1999;41:631–635, 1999. © 1999 Wiley-Liss, Inc.

Key words: wavelets, noise, Rician, SNR, wavelet-packets, denoising

INTRODUCTION

The signal-to-noise ratio (SNR) of an imaging system is a fundamental determinant of its spatial, temporal, and contrast resolution. Post-processing with conventional low-pass and rank statistic filters improves SNR but blurs edges considerably. Locally adaptive modeling techniques, such as wavelet packets, can perform better in this regard (1–5).

The denoising performance of principle-component methods, such as best-basis, wavelet packet algorithms, are degraded by non-Gaussian noise statistics; unfortunately, MR magnitude images demonstrate Rician noise (6). The Rician distribution varies dramatically with SNR; for an SNR of 0, it equals the highly skewed Rayleigh distribution, while for SNR > 5, it approximates a Gaussian distribution (6). While clinical images have overall SNR values exceeding 5:1, some important image features, particularly edge information, may have "local" SNRs < 5.

Fortunately, the noise statistics at the quadrature receivers are approximately Gaussian. We hypothesized that separately denoising the real and imaginary images before rectification should retain the SNR advantages of magnitude denoising in image areas with a local SNR > 5 while improving the denoising performance in areas with a local SNR < 5. This, in turn, should improve overall SNR, contrast-to-noise ratio (CNR), and edge depiction.

METHODS

Synthetic, phantom, and human images were studied.

Synthetic Images

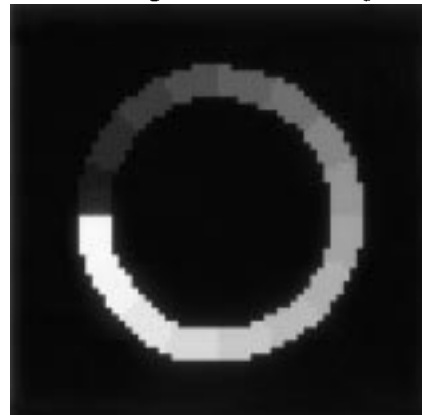
The synthetic images consisted of a 16-segment ring; the maximal amplitude was 16 at nine o'clock and decreased stepwise counterclockwise (Fig. 1A). The ring boundaries were traced from a "myocardial" phantom (Fig. 1B—see next section). Noisy complex images were formed as follows:

$$\text{Real} = \text{Magnitude} * \cos(\text{angle}) + N(0, \sigma); \quad [1]$$

$$\text{Imag} = \text{Magnitude} * \sin(\text{angle}) + N(0, \sigma); \quad [2]$$

where angle was chosen to be 30°. $N(0, \sigma)$ denotes the normal distribution with a mean of zero and standard

A. Segmented Ring



B. "Myocardial" Phantom

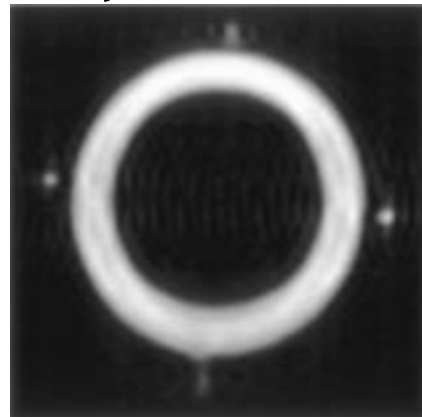


FIG. 1. **A:** Magnitude representation of noiseless ring image. **B:** "Myocardial" phantom at SNR ~100.

¹Section of Pediatric Cardiology, Children's Hospital at Yale–New Haven, New Haven, Connecticut

²Department of Diagnostic Radiology, Yale University School of Medicine, New Haven, Connecticut

*Correspondence to: Kevin M. Johnson, M.D., Department of Diagnostic Radiology, Yale University School of Medicine, Fitkin F7, 333 Cedar Street, New Haven, CT 06510.

E-mail: kevin.johnson@yale.edu

Received 27 March 1998; revised 23 July 1998; accepted 10 August 1998.

© 1999 Wiley-Liss, Inc.

deviation of sigma. Sigma was chosen such that SNR in the magnitude image ranged from 0.18 to 2.8.

Phantom Construction

Echoplanar images were collected from a “myocardial” phantom (Fig. 1B) constructed from three concentric Plexiglas cylinders with outer diameters of 82.5 mm, 69.9 mm, and 50.8 mm. Plexiglas thickness was 3.2 mm. The inner core and outer ring were filled with paraffin to decrease susceptibility artifact. The space between the two smaller cylinders contained 3.5% agarose gel doped with 4 mM NiCl. This simulated “myocardial wall” had a T2 of 22.5 ± 1 msec (0.5-tesla IBM minispectrometer) and an average thickness of 9.5 mm. To serve as resolution markers, four 3-mm ID plastic pipettes were filled with 0.5% agarose doped with 0.5 mM NiCl and cemented at equidistant intervals on the external surface of the 69.9-mm cylinder. Figure 1B demonstrates a high-resolution image with SNR of $\sim 100:1$.

Imaging

Phantom images were spin echo, echoplanar images made using resonant gradients (Advanced NMR, Wilmington, MA) and the body RF coil on a 1.5-tesla magnet (General Electric Signa, system 4.8). We used a TE of 20 of msec, a TR of 4000 msec, a field of view of $40 \text{ cm} \times 20 \text{ cm}$, an acquisition matrix of 128×80 , a display matrix of 256×128 , and a slice thickness of 3 mm. The segmented *k*-space gradient echo cine (FASTCARD, General Electric) used a

four-element phased-array torso coil. The four signals were denoised separately; each raw *k*-space data set was zero filled and fast Fourier transformed into a pair of real and imaginary images. The four pairs of images were combined into a single final image as follows:

$$I_{\text{total}} = \sqrt{I_1^2 + I_2^2 + I_3^2 + I_4^2} \quad I_j^2 = (I_{j \text{ real}}^2 + I_{j \text{ imag}}^2) \quad [3]$$

where I_{total} is the final reconstructed image and $I_{j \text{ real}}$ and $I_{j \text{ imag}}$ represent the quadrature components from receiver *j*, *j* = 1 to 4.

Wavelet Packet Denoising

The wavelet packet software was supplied by Woog and Coifman (5,7). Only a brief algorithm outline will be given here; details can be found in Coifman et al. (2) and Woog (5). There are three fundamental concepts in the algorithm: wavelet packet transformation, best-basis selection, and coefficient thresholding. For the sake of clarity, the following description is of the one-dimensional case, but the ideas hold as well for two dimensions.

In wavelet packet transformation, the original signal was transformed by a pair of quadrature mirror filters into two signal subspaces, to form the first level of the wavelet decomposition. This process was iterated on each subspace to form a complete tree of $\log_2(N)$ levels, where *N* is the length of the original signal. Each level was *N* elements (coefficients) long and was divided into subspaces. We

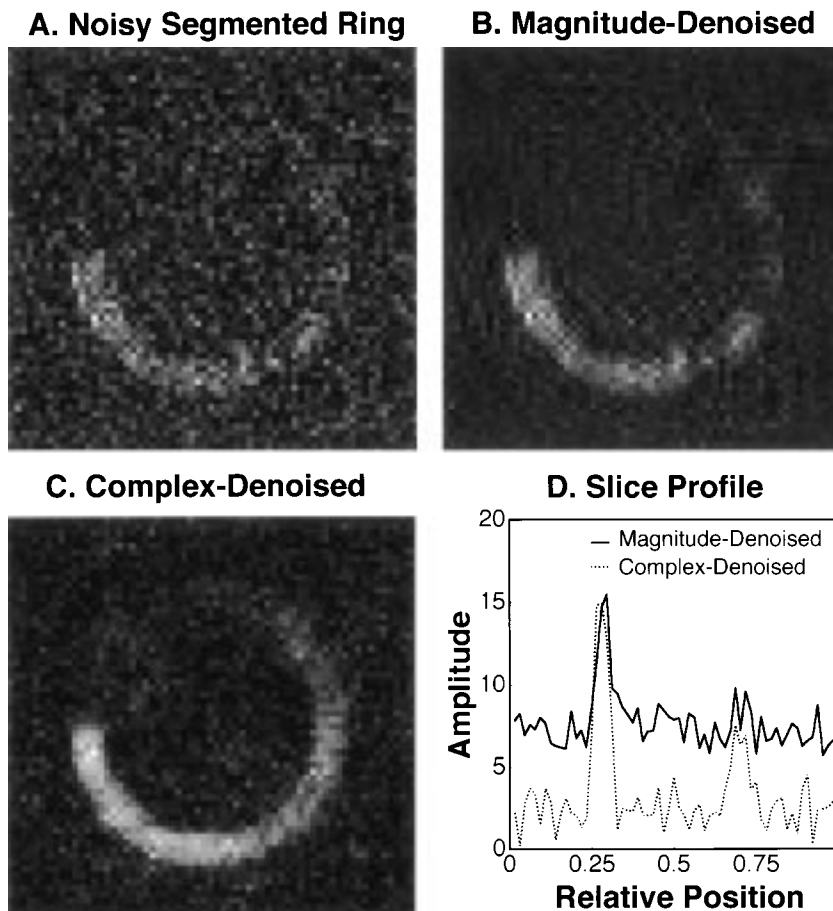


FIG. 2. **A:** A noisy ring image with a peak SNR of 2.7. **B:** Magnitude denoised ring image. **C:** Complex denoised ring image. **D:** Linear slice profile of B & C oriented from lower left corner to upper right corner. The complex-denoised image (dotted line) has better signal to background contrast.

used the filters for the 12-point “coiflet” wavelet, although, in theory, the optimal wavelet is image-dependent.

For best-basis selection, the complete tree had a redundancy of $\log_2(N)$. “Best-basis” selection consisted of finding the subtree that completely represents the original signal but that also concentrates the maximum amount of structured signal into the minimum number of coefficients. Gaussian noise is distributed evenly throughout the tree and will not concentrate in any particular subspace or in any particular coefficients within a subspace. This algorithm used a minimum entropy criterion to select the most compact basis. For thresholding, the coefficients were ranked by power, with signal coefficients having higher power relative to noise. A threshold value dividing “structure” from “noise” was defined using a “compressibility” or “spectral flatness” criterion (5).

Image Parameters

Image SNR was calculated using means and standard deviations calculated from two identical consecutive image acquisitions as follows:

$$\text{SNR} = \frac{\frac{1}{2}(\mu_1 + \mu_2)}{\frac{1}{\sqrt{2}}\sigma_{\text{diff}}} \quad [4]$$

where μ_1 and μ_2 are the region of interest (ROI) means from images 1 and 2, respectively, and σ_{diff} is the ROI standard deviation from the difference image. ROIs were chosen exactly in the synthetic images and by manual tracing in the phantom and human images, taking care to avoid edge effects.

For magnitude images with $\text{SNR} < 5$, ROI mean values are biased upward, leading to SNR overestimation. Three correction methods have been proposed: nomograms, power images, and background subtraction (6). Unfortunately, the processed images no longer observe Rician statistics, making it impossible to accurately calculate SNR or CNR improvement. Consequently, denoising efficacy must be inferred by relative changes in mean and standard deviation.

To characterize the edge sharpness for the “myocardial” phantom, full-width, half-maximum (FWHM) and edge width (EW, defined as the distance between the 25th and 75th percentile) were calculated radially at three-degree increments about the phantom centroid. First, the “epicardial” and “endocardial” borders were manually traced and fit to a cubic spline. From the epicardial border, the centroid was derived and used to convert the image to polar coordinates using bicubic interpolation. Along each radius, the FWHM and the rise and fall widths were calculated. EW was calculated as the average of the rise and fall widths.

RESULTS

Figure 2A demonstrates the original noisy ring image (peak SNR of 2.7:1); the wall may be tracked counterclockwise from nine o'clock (at its maximal intensity) to about three

o'clock before noise obscures it. In the complex denoised image (Fig. 2C), the wall is visibly sharper and more homogeneous, and it can be tracked for a greater distance than in the original and in the magnitude denoised image (Fig. 2B). The background noise in the complex denoised image is less structured, streaky, and “block-like” than in the magnitude denoised image. The magnitude denoised ring is broader than the complex denoised ring and has poorer signal-to-background contrast (Fig. 2D).

Figure 3 demonstrates the means and variances for the 16 zones at baseline (Fig. 3A) and following complex and magnitude denoising (Fig. 3B). The Rician DC bias was unimportant at high SNR but degraded low-intensity component resolution in the original and magnitude denoised image. Complex denoising greatly reduced the mean bias and tracked the sector means to an $\text{SNR} < 1$. Although noise suppression was grossly similar for both techniques, the results from complex denoising were more homogeneous. Magnitude denoising produced higher standard deviation for sectors with $\text{SNR} > 1.35$ and lower values for sectors with $\text{SNR} < 1.35$. This discrepancy likely reflects the original disparity in noise power arising from rectification.

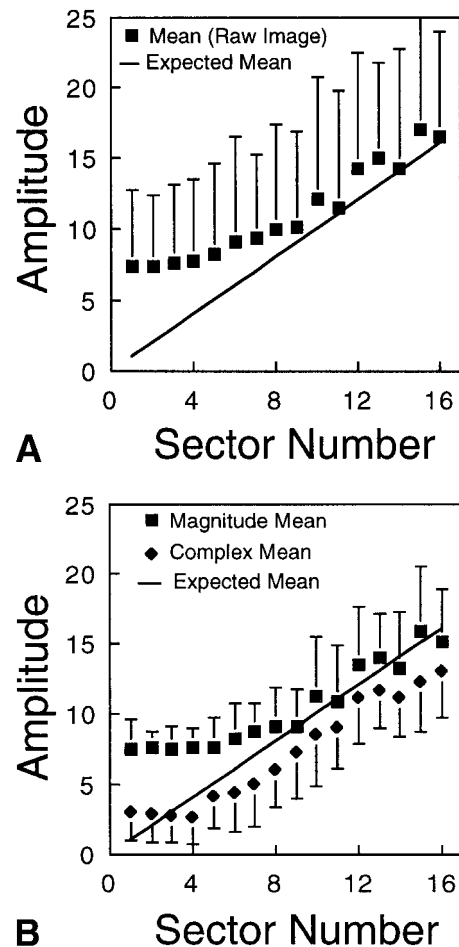


FIG. 3. **A:** Sector mean (squares) and standard deviation for the raw image (error bar = 1σ). Solid line demarcates the expected value. **B:** Mean and standard deviation for magnitude denoising (squares) and complex denoising (diamonds). Solid line demarcates the expected value.

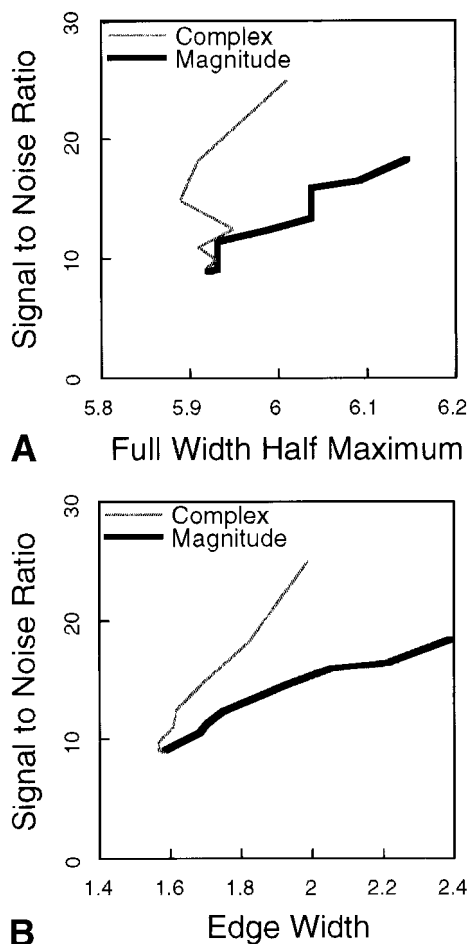


FIG. 4. Plot of SNR improvement versus full-width, half-maximum (A) and edge width (B). As threshold stringency increases, SNR improves, but FWHM and EW increase.

To assess whether complex denoising yielded sharper edges in real images, single-shot echoplanar myocardial phantom images (SNR of 8.8) were denoised and edge properties assessed. To ensure a fair comparison between techniques, the improvement in blurring per unit SNR was determined over a large threshold range. Figure 4 demonstrates the SNR improvement versus the FWHM and EW for magnitude and complex denoising. For any given SNR improvement, complex denoising produced less FWHM or EW broadening. This effect disappeared, however, if the initial SNR was improved by signal averaging. In fact, the two techniques produced virtually identical traces for both FWHM and EW for SNR > 16 (not shown).

Figure 5 demonstrates results for a single, noisy, segmented k -space gradient echo cine frame of a human heart. Both the magnitude and complex denoised images show increased detail in the chest wall, endocardial contours, and epicardial regions. The complex denoised images have better background suppression, resulting in sharper pericardial and myocardial definition. In a close-up view of the interventricular groove, the denoised images reveal an epicardial vessel invisible on the original image.

DISCUSSION

Wavelet packet denoising improves MR image SNR, sometimes strikingly, without compromising object edges. The Rician noise statistics of magnitude images degrade edge and contrast resolution; denoising before signal rectification drastically reduces these phenomena. Results were demonstrated quantitatively in synthetic and phantom images and qualitatively in human images. The nonzero mean of rectified white noise biases the background of magnitude images (6), thereby decreasing low-intensity object contrast. Unlike magnitude denoising, complex denoising avoids this bias (Figs. 2 and 3). Complex denoising also improves edge depiction because it avoids the effects of uneven distribution of noise across the image caused by rectification (Fig. 4).

Wavelet transforms (not wavelet packets) have also been used to denoise MRI images (8,9); however, the influence of Rician statistics was not examined. In general, wavelet packet algorithms find a more "compact" signal representation than single-basis wavelet decomposition. Although

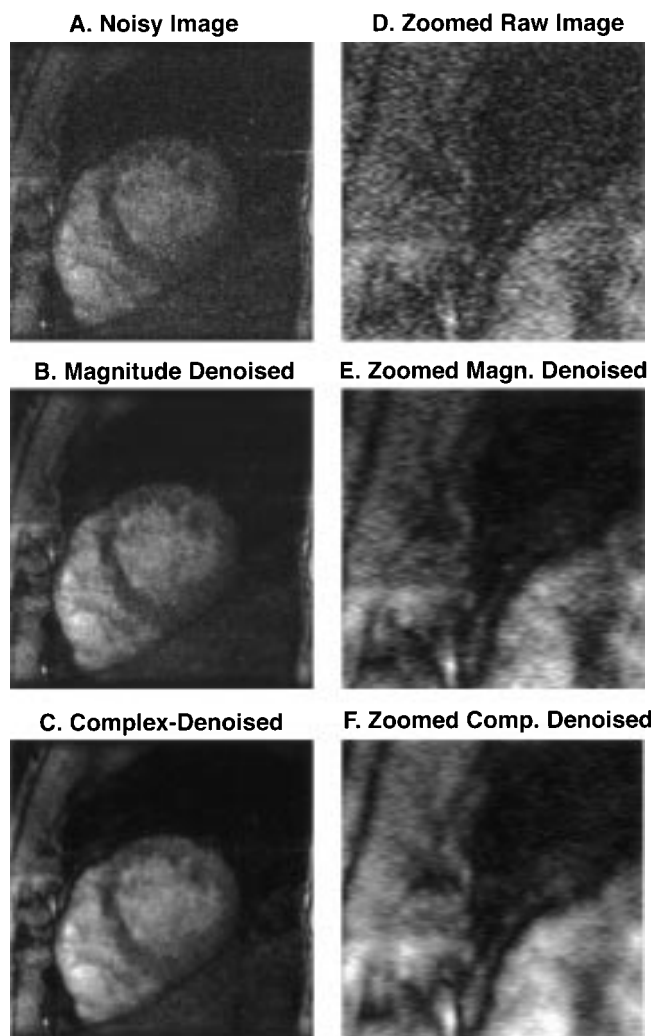


FIG. 5. Segmented k -space gradient echo cine (FASTCARD) frame of the heart at end diastole. **A**: Original image. **B,C**: Magnitude denoised and complex denoised images, respectively. **D,E,F**: "Zoomed" images of the interventricular groove.

wavelet packet denoising has been applied to acoustic well logging, synthetic aperture radar, and image-processing problems (1, 2, 5, 7), little work has appeared in the medical literature to date (3,4).

Limitations

If quadrature images contain complicated high-frequency phase oscillations, magnitude denoising may have a "tighter" basis than complex denoising and achieve more significant noise reduction. The most common cause of these oscillations, however, is inaccurate centering of the k -space data, which is easily corrected. Medical images are two-dimensional low-pass functions in k space; centering the k -space modal frequency before Fourier reconstruction ensures low-frequency quadrature variation.

For actual MRI images, complex images required a lower compression threshold than magnitude images to achieve comparable SNR improvement, because their best bases and noise statistics were different. To decouple the threshold selection problem, it was important to index SNR improvement to edge properties. This was straightforward in the phantom images but was not possible in the human images. Nevertheless, the qualitative results in humans were quite concordant with predictions based upon the phantom images.

Conclusions

Wavelet packets can significantly improve image SNR without compromising edge sharpness. Rician noise properties degrade denoising performance in regions where local SNR is < 5 . Peak or average SNR over an entire image may not reflect the situation at edges and near low-contrast objects. The results of this study should generalize to

higher-dimensional denoising (5); three-dimensional data sets for coronary artery imaging may be particularly well suited to this technique. Determination of the diagnostic utility of wavelet packet denoising ultimately will require formal receiver operator characteristic (ROC) studies.

ACKNOWLEDGMENTS

We are grateful to Drs. R.R. Coifman and Lionel Woog for the donation of software and expertise and to Dr. Roland Guglielmi for helpful discussions.

REFERENCES

1. Coifman RR, Wickerhauser MV. Entropy-based algorithms for best basis selection. *IEEE Trans Inf Theory* 1992;38:712-718.
2. Coifman RR, Wickerhauser MV. Adapted waveform analysis as a tool for modelling, feature extraction, and denoising. *Opt Eng* 1994;33:2171-2174.
3. Johnson KM, Kayser HWM, Guglielmi R, et al. Wavelet denoising of echoplanar MR images. In: *Second Annual Meeting of the Society of Magnetic Resonance*. San Francisco: Society of Magnetic Resonance, 1994. p. 799.
4. Wood JC, Johnson KJ. Wavelet-packet denoising of echoplanar and FAST-CARD images. In: *First Annual Meeting of the Society for Cardiovascular Magnetic Resonance*. Atlanta: Society of Cardiovascular Magnetic Resonance, 1997. p. 79.
5. Woog L. Adaptive waveform algorithms for denoising. Ph.D. thesis, Department of Computer Science, Yale University, 1996.
6. Gudbjartsson H, Patz S. The Rician distribution of noisy MRI data. *Magn Reson Med* 1995;34:910-914.
7. Coifman RR, Wickerhauser MV, Woog L. Adaptive design toolkit software. New Haven: Fast Mathematical Algorithms and Software Corporation; 1997.
8. Weaver JB, Xu Y, Healy DM Jr, Cromwell LD. Filtering noise from images with wavelet transforms. *Magn Reson Med* 1991;21, 288-295.
9. Xu Y, Weaver JB, Healy DM, Lu J. Wavelet transform domain filters: a spatially selective noise filtration technique. *IEEE Trans Image Proc* 1994;3:747-758.